Applied Catalysis B: Environmental 245 (2019) 197–206

Contents lists available at ScienceDirect

Applied Catalysis B: Environmental

journal homepage: www.elsevier.com/locate/apcatb

Fabrication of high photoreactive carbon nitride nanosheets by polymerization of amidinourea for hydrogen production

Jinshui Cheng[a,b], Zhao Hu[b], Qin Li[b], Xiaofang Li[a,**], Shun Fang[b], Xiaofeng Wu[b], Mei Li[b], Yaobin Ding[b], Bing Liu[b], Changjun Yang[b], Lili Wen[c], Yi Liu[a,d], Kangle Lv[a,b,*]

[a] College of Chemistry and Chemical Engineering, Wuhan University of Science and Technology, Wuhan, 430081, PR China
[b] Key Laboratory of Catalysis and Materials Science of the State Ethnic Affairs Commission & Ministry of Education, Hubei Province, College of Resources and Environmental Science, South-Central University for Nationalities, Wuhan, 430074, PR China
[c] Key Laboratory of Pesticide & Chemical Biology of Ministry of Education, College of Chemistry, Central China Normal University, Wuhan, 430079, PR China
[d] College of Chemistry and Molecular Sciences, Wuhan University, 430072, PR China

ARTICLE INFO

Keywords:
Carbon nitride
Nanosheet
Amidinourea
Visible
Photoreactivity
Hydrogen production

ABSTRACT

As a typical visible-light-responsive organic semiconductor photocatalyst, graphitic carbon nitride (gCN) only exhibits moderate photoreactivity beacuse of its low specific area, limited light harvesting ability and quick recombination of photo-generated carriers. Herein, we report the fabrication of gCN nanosheets (gCN-NSs) with large BET surface area, excellent visible-light-absorptive property and efficient separation of carriers by direct polymerization of amidinourea, the product from the hydrolysis of dicyandiamine (DCDA). When compared with that of bulk gCN (S0) synthesized by direct polymerization of DCDA, the visible photocatalytic hydrogen evoluation rate of gCN-NSs (S2 sample) obtained by condensation of amidinourea improved 4.9 times, which is also 2.4 times higher than that of gCN-NSs (Su sample) which is prepared by polymerization of urea. The enhanced visible photocatalytic activity gCN-NSs (S2) toward hydrogen production can be ascribed to the combined effects of enlarged BET surface that provides more active sites for adsorption and photocatalytic reaction, compacted π-π layer stacking which facilitates the efficient separation of photo-generated carriers, negatively shifted CB potential and improved hydrophilic property that favor the electron transfer at the interfaces between gCN and water. In addition, the product yield of gCN-NSs (S2 sample) from the polymerization of amidinourea is 11.9%, which is 10.8 times higher than Su sample that prepared from urea (only 1.1%).

1. Introduction

As a typical organic polymeric semiconductor photocatalyst, graphitic carbon nitirde (gCN) has attracted much attention due to its biocompatibility and visible-light-responsive property [1–3], which is promising to solve the problems related to environmental pollution and energy crisis such as photocatalytic oxidation of organic pollutants in water [4–7], air purification [8–10], photoreduction of CO_2 to proudce hydrocarbon fuels [11–14] and water splitting for hydrogen production [15–18]. However, gCN suffers from the low BET surface area, poor dispersion in water, quick recombination of the photo-generated carriers, and/or limited visible-light-responsive range, which therefore hamper the practical application [16,17,19–23].

Exfoliation of bulk gCN to gCN nanosheets (gCN-NSs) can not only increase the BET surface area, but also facilitate the migration of photo-generated carriers of the photocatalyst, enhancing the photoreactivity [24,25]. However, the yields of gCN-NSs by oxidative exfoliation of bulk gCN are very low (about 5–6% base on bulk gCN), and the process for exfoliation is energy-consuming due to the repeated calcination at high temperature [26,27]. When compared with oxidative exfoliation, sonicated exfoliation seems energy-saving, but on the expense of longer time (more than 10 h) and lower yields [28–30]. To improve the yield of gCN-NSs, organic solvent such as γ-valerolactone was added into the bulk gCN during sonicated treatment [31]. However, it is very hard to remove the residue γ-valerolactone from the surface of the obtained gCN-NSs, restraining the applications of gCN-NSs. Recently, ball milling was also

* Corresponding author at: College of Chemistry and Chemical Engineering, Wuhan University of Science and Technology, Wuhan, 430081, PR China.
** Corresponding author.
E-mail addresses: xfli@whu.edu.cn (X. Li), lvkangle@mail.scuec.edu.cn (K. Lv).

https://doi.org/10.1016/j.apcatb.2018.12.044
Received 16 September 2018; Received in revised form 8 December 2018; Accepted 16 December 2018
Available online 17 December 2018

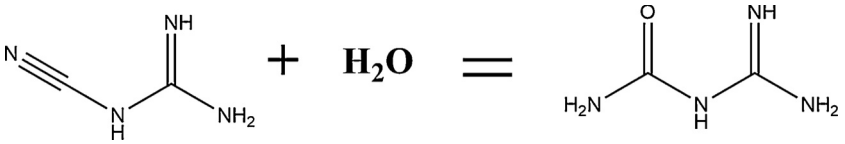

Scheme 1. Preparation of amidinourea by hydrolysis of dicyandiamine.

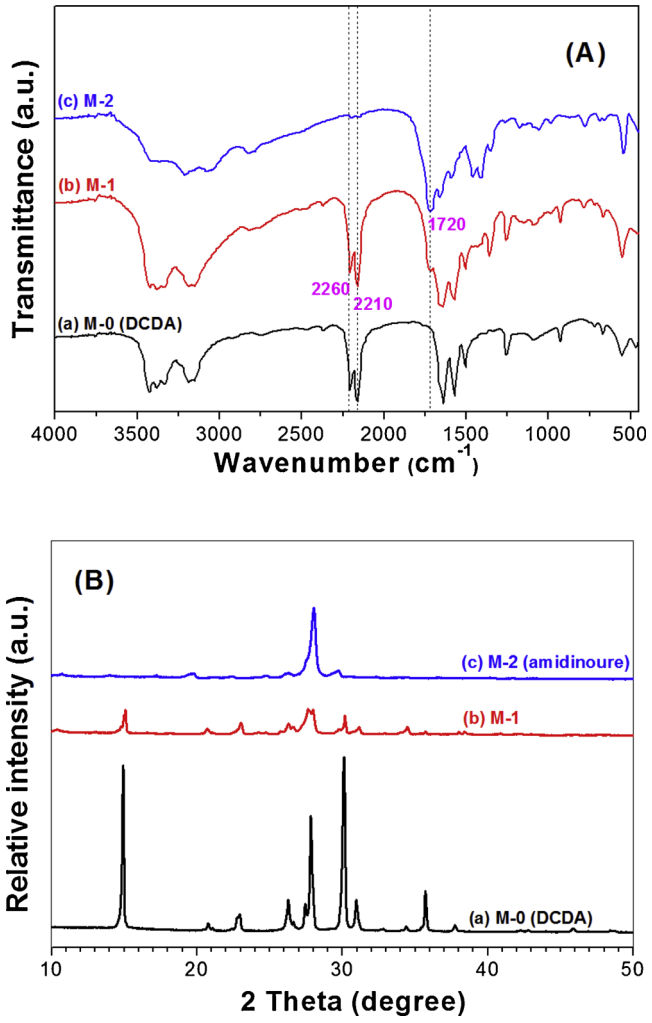

Fig. 1. FT-IR spectra (A) and XRD patterns (B) of the precursors for carbon nitride photocatalysts.

used for the exfoliation of bulk gCN. Unfortunately, only gCN-NSs with small sizes (2–6 nm in size) can be obtained due to the mechanical destruction [32]. Therefore, efficient fabrication of gCN-NSs with high quality is highly desired but it still remains a great challenge [33].

Dicyandiamine ($C_2H_4N_4$, DCDA) is one of the widely used starting materials for the synthesis of bulk gCN, which exhibits good visible-light-responsive range with an absorption edge of up to 450 nm [21,26]. However, the BET surface area of the bulk gCN from the polymerization of DCDA is very small (about 10 $m^2 g^{-1}$) [21]. On considering that sheet-like gCN was obtained when polymerization of urea (CH_4N_2O) [34–37], we believe that using the oxygen-containing precursor can reduce the interaction between π–π stacking layers of gCN, which therefore favors for the production of sheet-like gCN (gCN-NSs). In this study, we tried to obtain gCN-NSs by direct polymerization of amidinourea ($C_2H_6N_4O$), a oxygen-containing precursor from the hydrolysis of DCDA (Scheme 1) [38,39]. When compared with urea, the conjugated effect in amidinourea is much stronger. Then it can be predictable that the gCN-NSs prepared from amidinourea will exhibit broader visible-light-responsive range than that from urea, which therefore benefits its photoreactivity.

2. Experimental

2.1. Hydrolysis of dicyandiamine (DCDA) to produce amidinourea

1.5 g of DCDA (M-0) was dissolved in 65 mL of water, which was then transferred into a 100 mL Teflon-lined autoclave and kept at 200 °C for 1 h (M-1 sample) or 2 h (M-2 sample). After cooling to room temperature, white powders (M-1 or M-2 sample) were obtained by rotary distillation.

2.2. Preparation of carbon nitride

Graphitic carbon nitride (gCN) was prepared by calcination 50 mL of crucible containing 12.0 g of the precursor at 550 °C for 4 h under air condition with a ramp rate of 5 °C min^{-1}. The products were named as S0, S1, S2 when M-0 (DCDA), M-1 and M-2 were used as precursor, respectively.

For comparison, gCN (Su) was also prepared by calcination 12.0 g of urea under other identical conditions.

2.3. Characterization

The X-ray diffraction (XRD) patterns were obtained on a D8-advance X-ray diffractometer (German Bruker). The morphology of the photocatalyst was observed on a transmission electron microscope (TEM) (Tecnai G20, USA) and a field emission scanning electron microscope (SEM) (S-4800, Hitachi, Japan). FT-IR spectrum was recorded on a NEXUIS-470 infrared spectrometer (Nicolet Co., U.S.A.). Nitrogen adsorption-desorption isotherms were obtained on an ASAP 2020 (Micromeritic Instruments, USA) nitrogen adsorption apparatus. All the samples were degassed at 200 °C prior to measurements. X-ray photoelectron spectroscopy (XPS) measurements were performed with a Multilab 2000 XPS system with a monochromatic Mg K*α* source and a charge neutralizer. All of the binding energies were referenced to the C 1 s peak at 284.6 eV of the surface adventitious carbon. UV–vis absorbance spectrum was obtained for the dry-pressed disk samples with a UV–vis spectrophotometer (UV-2550, Shimadzu, Japan). Photoluminescence (PL) spectrum was measured on a Fluorescence Spectrophotometer (F-7000, Hitachi, Japan). The excitation wavelength was 380 nm, the scanning speed was 1200 nm min^{-1}, and the PMT voltage was 400 V. The width of excitation slit and emission slit were both 10.0 nm.

2.4. DFT calculation

All spin-polarized DFT-D2 calculation was conducted in “Vienna Ab-

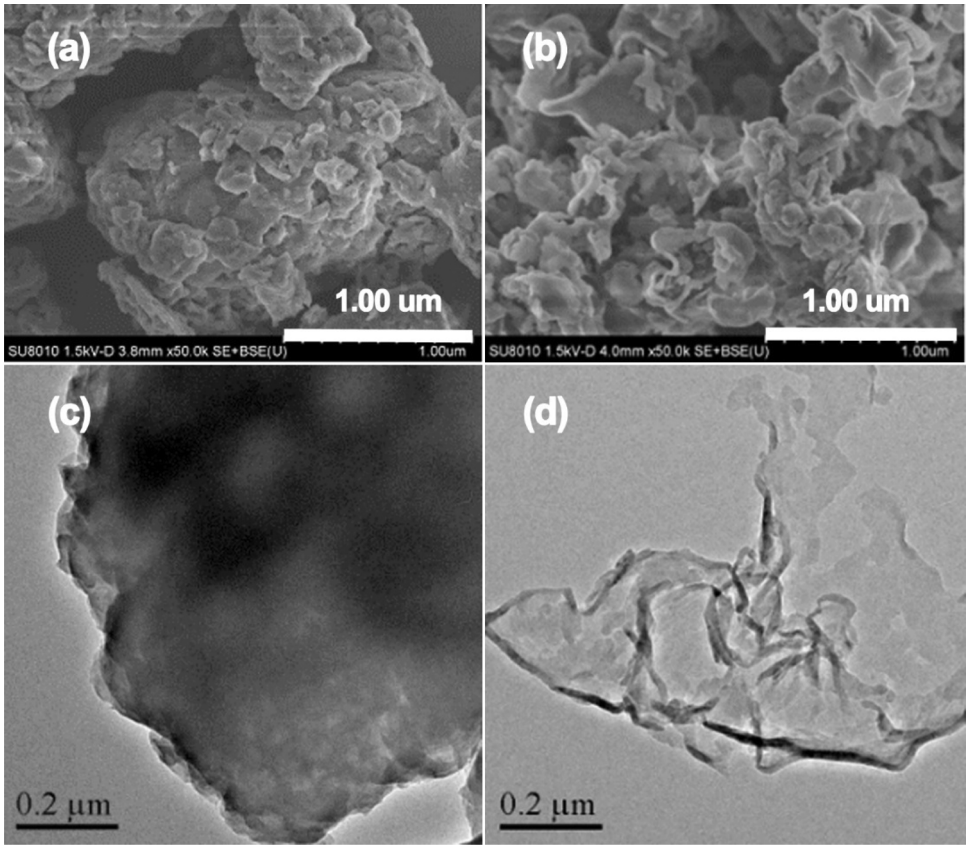

Fig. 2. SEM and TEM images of S0 (a and c) and S2 (b and d) samples.

initio Simulation Package" (VASP code 5.4.1) through the generalized gradient correlation function. Cut-off energy and Gaussian trailing width were set to be 400 eV and 0.2 eV, respectively. The Bril-louin zone was adopted by a 3 × 3 × 1 Monkhorst Pack grid. All structures and energy were converged to below 0.01 eV A 2 × 2 × 3 supercell of bulk g-C_3N_4 was first relaxed. 3-layered and 1-layered CN plane were used as bulk g-CN (S0) and gCN-NSs (S2), respectively.

2.5. Photoelectrochemical measurements

Transient photocurrent, electrochemical impedance spectroscopy (EIS) Nyquist plots and Mott-Schottky plots were carried out on an Electrochemical Station (CHI660, China). A collimated light beam from an LED lamp emitted mainly at 420 nm (3 W, Shenzhen LAMPLIC) was used for excitation of the ITO/gCN electrode. These measurements were carried out with a standard three-electrode assembly. The ITO/gCN electrode, Pt plate, and Ag/AgCl electrode were used as the working, counter, and reference electrodes, respectively. Na_2SO_4 (0.4 mol L^{-1}) is used as the electrolyte.

2.6. Detection of radicals by electron spin-resonance spectroscopy

Electron spin resonance (ESR) signals of radicals spin-trapped by 5,5-dimethyl-1-pyrroline N-oxide (DMPO) were recorded on a spectrometer (JES FA200). Specimens for ESR measurement were obtained by mixing the photocatalysts in a 40 mM DMPO solution tank (methanol dispersion for DMPO-·OOH/$O_2{\cdot}^-$ and aqueous dispersion for DMPO-·OH) and illuminated with visible LED lamp (λ = 420 nm).

2.7. Photocatalytic hydrogen production

50 mg of gCN photocatalyst was suspended in 80 mL mixed solution containing 8 mL of triethanolamine, 72 mL of deionized water and 150 u L of $H_2PtCl_6{\cdot}6H_2O$ aqueous solution (10 g L^{-1}) to load 1.0 wt.% of Pt on the surface of the catalysis. Prior to irradiation, the reactor was purged with N_2 to remove dissolved oxygen. Then a 350 W Xenon arc lamp with a UV-cutoff filter (≥ 420 nm) was used to trigger the photocatalytic reaction. The amount of hygrogen gas was monitored by a gas chromatography with 5 Å molecular sieve column (GC2018, Shimadzu, Japan). Each experiment for photocatalytic hydrogen production was repeated for 3 times.

3. Results and discussion

3.1. Structures of the starting materials

From the infrared spectra of Fig. 1A, two strong peaks centering at 2260 and 2210 cm^{-1} can be clearly seen for DCDA sample (M-0), which are typical infrared vibration of cyano group (RC≡CR). After hydrolysis for 1 h (M-1), the two peaks still exist. At the same time, a new peak centering at 1720 cm^{-1} appears, which is the characteristic vibration of carbonyl group (−C═O) in amide, indicating the transformation of DCDA. After reaction for 2 h, the absorption peaks of cyano group for M-2 sample disappears and the peak of carbonyl group becomes much stronger, suggesting the totally transformation of DCDA to amidinourea (Scheme 1). The transformation of DCDA to amidinourea can also be reflected from the corresponding powder XRD characterization results

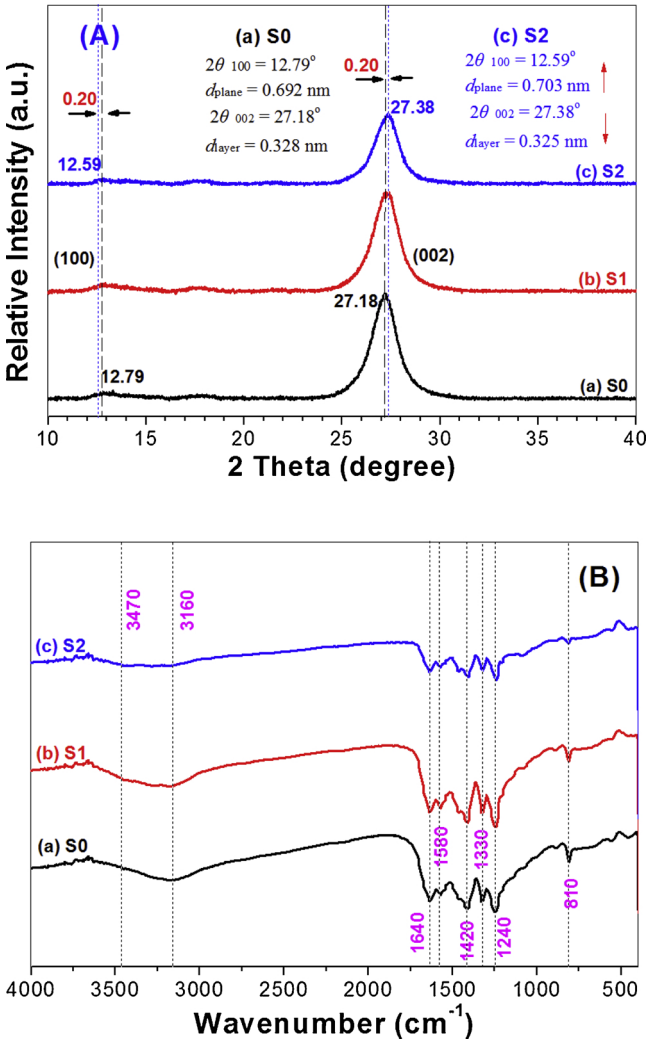

Fig. 3. XRD patterns (A) and FT-IR spectra (B) of the prepared gCN photocatalysts.

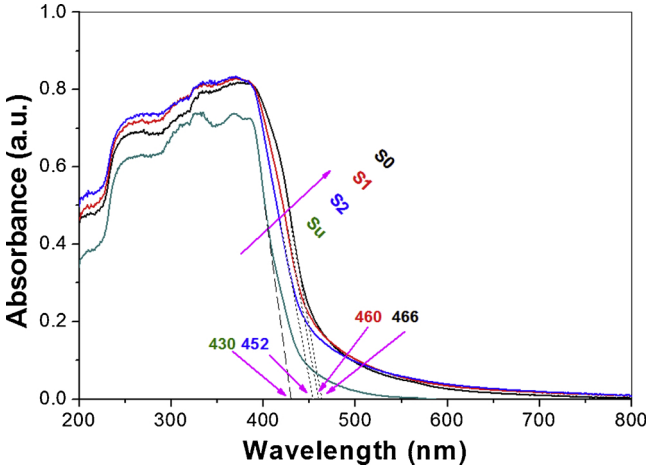

Fig. 4. Uv–vis diffuse reflectance spectra (DRS) of the prepared gCN photocatalysts.

Table 1
Physical property of the photocatalyst.

Photocatalyst	Nitrogen sorption			Bandgap (eV)
	S_{BET} ($m^2 g^{-1}$)	PV ($cm^3 g^{-1}$)	APS (nm)	
S0	12.2	0.056	16.9	2.66
S1	28.8	0.136	18.5	2.70
S2	59.8	0.282	20.5	2.74
Su	118.6	0.446	16.2	2.88

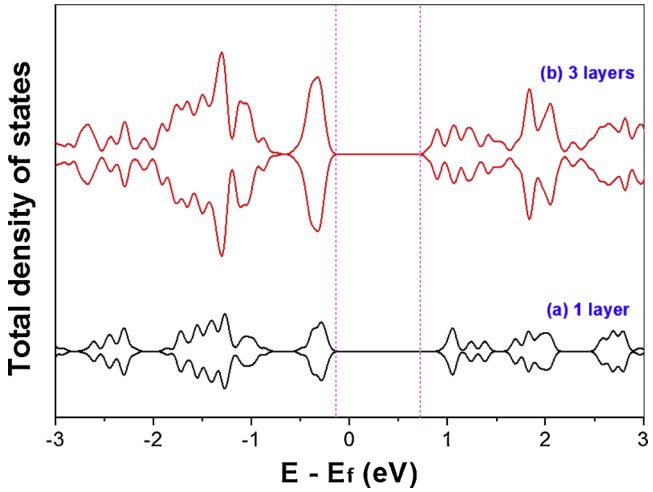

Fig. 5. Comparison of the calculated band structures between 1-layered (a) and 3-layered (b) gCN photocatalysts.

(Fig. 1B), where DCDA (S0) and amidinourea (S2) exhibits totoally different XRD patterns.

3.2. Morphology of gCN

The bulk structure of gCN obtained from the calcination of DCDA can be clearly seen from the SEM and TEM images (Fig. 2a and c), this is due to the strong π–π interaction between stacking layers [26]. The transport of photo-generated charge carriers between layers of bulk gCN is very difficult because of the high potential barriers between the layers (33.2 eV), which results in a poor photoreactivity [26]. As expected, sheet-like gCN was formed by polymerization of amidinourea (Fig. 2b and Fig. 2d). In addition, the gCN-NSs are in large size (micrometer scale). Therefore, by using oxygen-containing amidinourea as starting material, we successfully synthesized gCN-NSs with large sizes. The exposure of the basal planes of gCN-NSs can not only increase the number of active site due to the enlarged BET surface area, but also sharply reduce the diffusion distance of the photo-generated acrriers, which is beneficial to the photoreactivity [23,40].

According to our experimental results, the yield for the production of gCN-NSs using amidinourea as starting material was 11.9%, which is 10.8 times higher than that of gCN-NSs from the polymerization of urea (yield of only 1.1%)

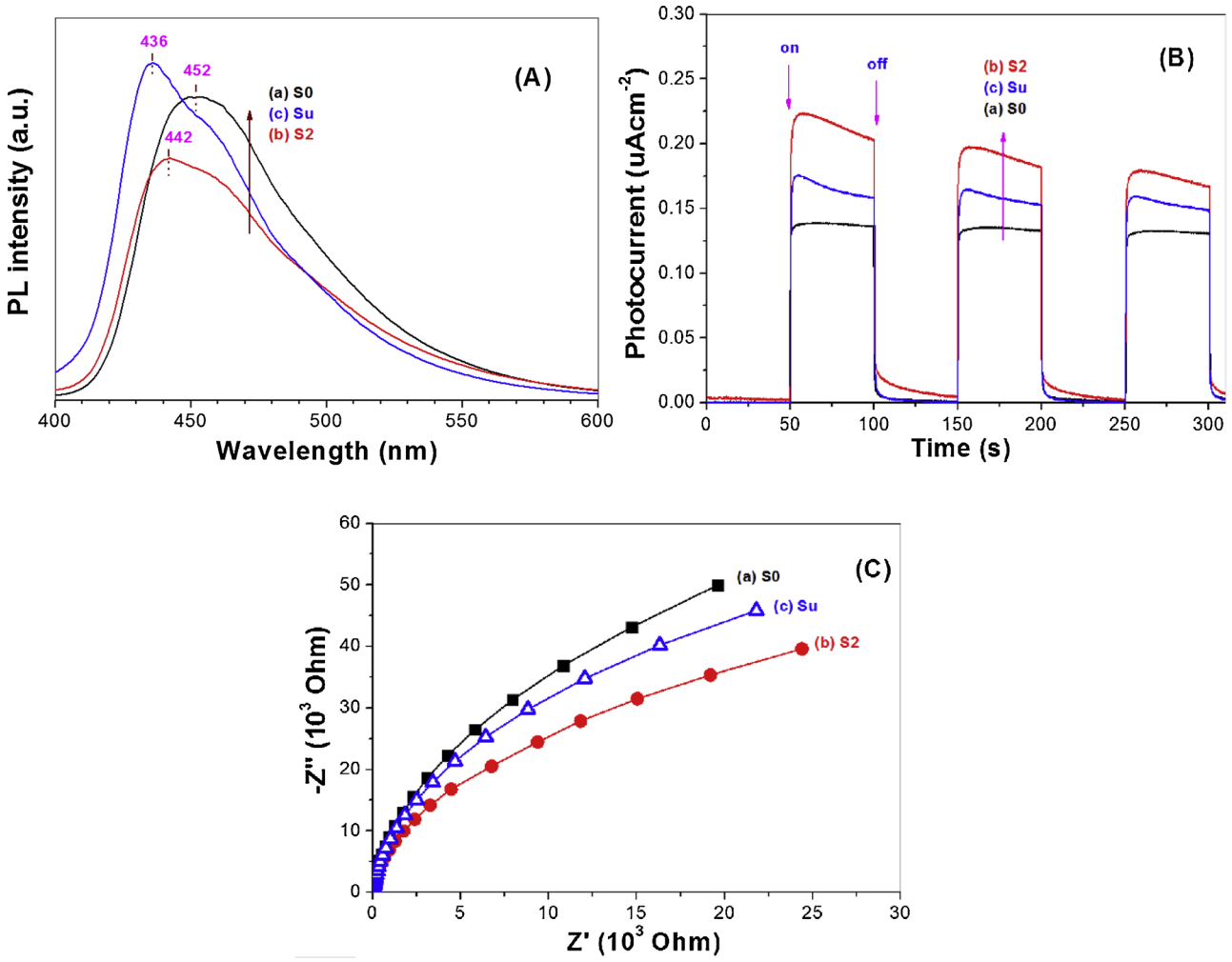

Fig. 6. Comparison of the photoluminescence (PL) spectra (A), Photocurrents (B) and EIS Nynquist plots (C) of the prepared gCN photocatalysts.

3.3. XRD and FTIR spectra of gCN samples

Fig. 3A compares the XRD patterns of the photocatalysts obtained by polymerization of DCDA before (S0 sample) and after hydrolyzed for 1 h (S1 sample) and 2 h (S2 sample), respectively. We can clearly see that all the samples have a strong peak centering at 27° and a weak peak located at 13°, corresponding to (100) and (002) planes of carbon nitride originated from the interplanar packing of heptazine units and π–π interlayer stacking motif, respectively [6,41,42]. When compared with that of S0 sample, the (002) peak intensity of S2 sample is much weaker, reflecting the exfoliation of bulk gCN for S2 sample, which is consistent with the SEM and TEM images (Fig. 2). Carefully view shows that, in comparison with that of S0 sample, the (002) peak of S2 sample shifts upward from 27.18° to 27.38°, while the (100) peak shifts downward from 12.79° to 12.59°, reflecting the compacted interlayer stacking distance (from 0.328 nm to 0.325 nm) and an extended interplanar packing distance (from 0.692 nm to 0.703 nm). This will facilitate the charge diffusion between layers and within the plane, enhancing the photoreactivity of gCN [21].

The structure of gCN was further confirmed by FTIR spectrum as shown in Fig. 3B, where the absorption at 1640, 1580, 1420, 1330 and 1240 cm^{-1} were attributed to the vibrations of (C═N) or (C—N), the typical stretching modes of CN heterocycles. The absorption at 810 cm^{-1} is the characteristic mode of the triazine units, and the broad bands in the range of 3100-3500 cm^{-1} are attributed to the vibration modes for —NH of gCN [15].

3.4. Optical and (photo)electrochemical measurements

Light harvesting ability is of great importance to the photocatalytic activity of the photocatalyst [16,43]. Fig. 4 compares the UV–vis absorption spectra of different photocatalysts. It can be seen that the absorption edge of gCN steady blue-shifts from 466 (S0) to 460 (S1) and 452 nm (S2) with increase in the hydrolysis time of DCDA, reflecting the broadened bandgap of gCN-NSs than that of bulk gCN (Table 1). This is because of the quantum size effect.

Fig. 5 displays the calculated density of states (DOS) of gCN photocatalyst. It can be seen that the band gap of 1 layered-gCN (representing gCN-NSs) is larger than that of 3-layered gCN (representing bulk gCN), consistent with the observation in Fig. 4 [8].

From Fig. 4, it can be also seen that S2 sample exhibits broader light-responsive range than Su sample (gCN prepared by direct

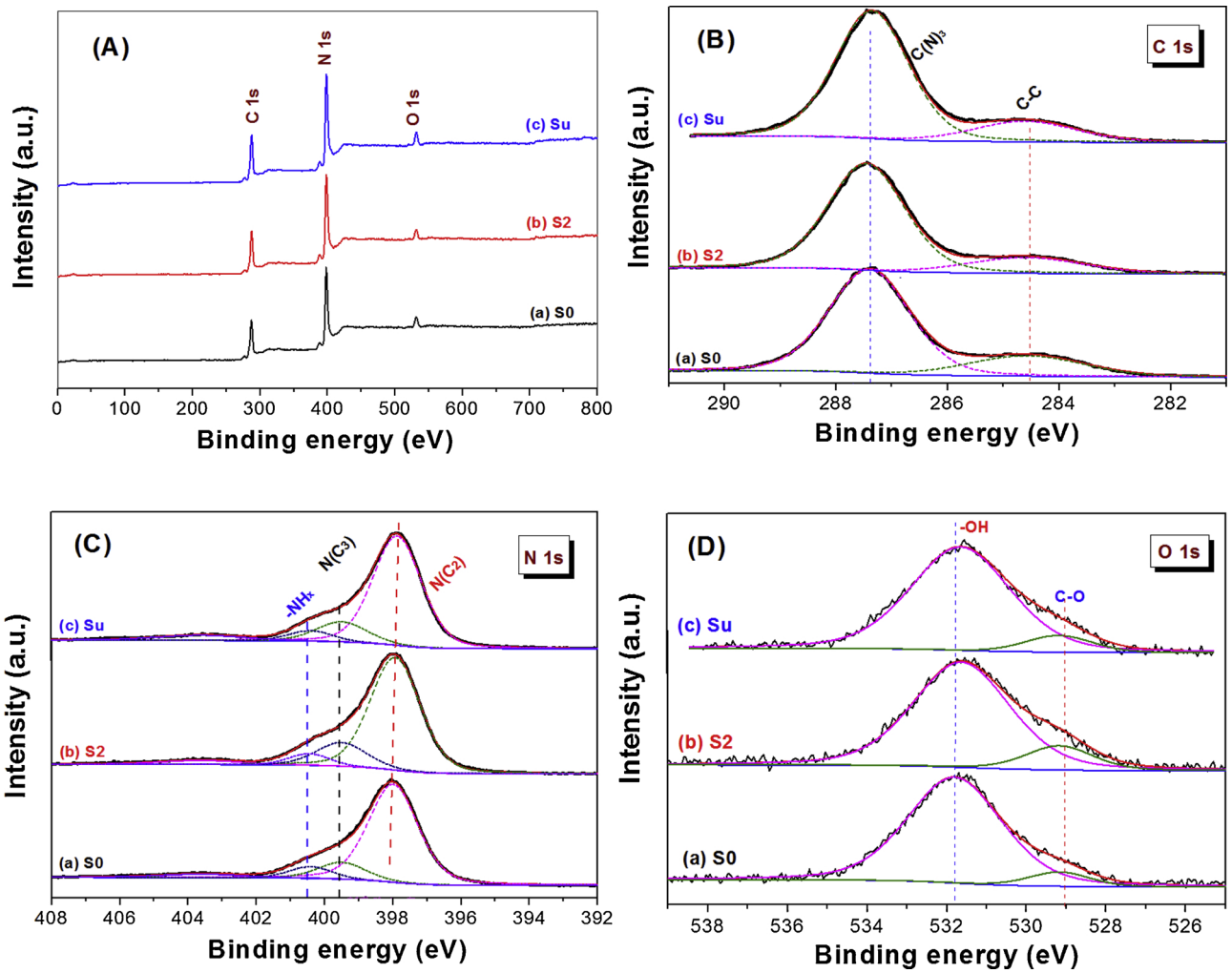

Fig. 7. XPS survey spectra (A) and high resolution XPS spectra in C 1 s (B), N 1 s (C) and O 1 s (D) regions of the photocatalysts.

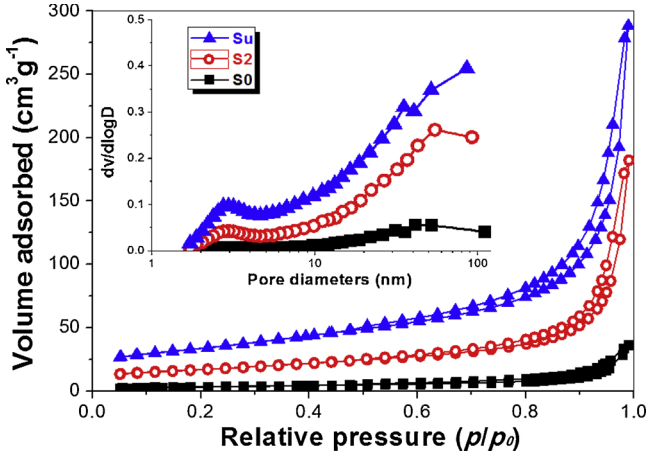

Fig. 8. Nitrogen sorption-desorption isotherms and the corresponding pore size distribution curves (inset) of the prepared gCN photocatalysts.

polymerization of urea), which exhibits an absorption edge of only 430 nm.

Photoluminescence (PL) was used to evaluate the recombination rate of photo-generated carriers. From Fig. 6A, it can be seen that the PL intensity of S2 gCN-NSs is the weakest among three gCN photocatalysts. The weaker PL intensity means the slower recombination rate of photo-generated electron-hole pairs [44,45].

We further examined the transient photocurrent of the photocatalyst under visible light illumination ($\lambda > 420$ nm). As can be seen from Fig. 6B that S2 gCN-NSs possesses the highest photocurrent among all the photocatalysts, indicating its fastest charge separation efficiency [46,47]. The smallest arc radius of S2 gCN-NSs in EIS also confirms its fastest interfacial charge transfer in the electrode/electrolyte interface (Fig. 6C) [7,47–49]. Therefore, the high photoreactivity of S2 gCN-NSs can be predictable.

3.5. XPS and reactive oxygen species (ROSs)

XPS was used to determine the chemcial states of the elements for gCN photocatalyst. From the XPS survey spectra shown in Fig. 7A, it can be seen that all gCN samples contain C and N elements,

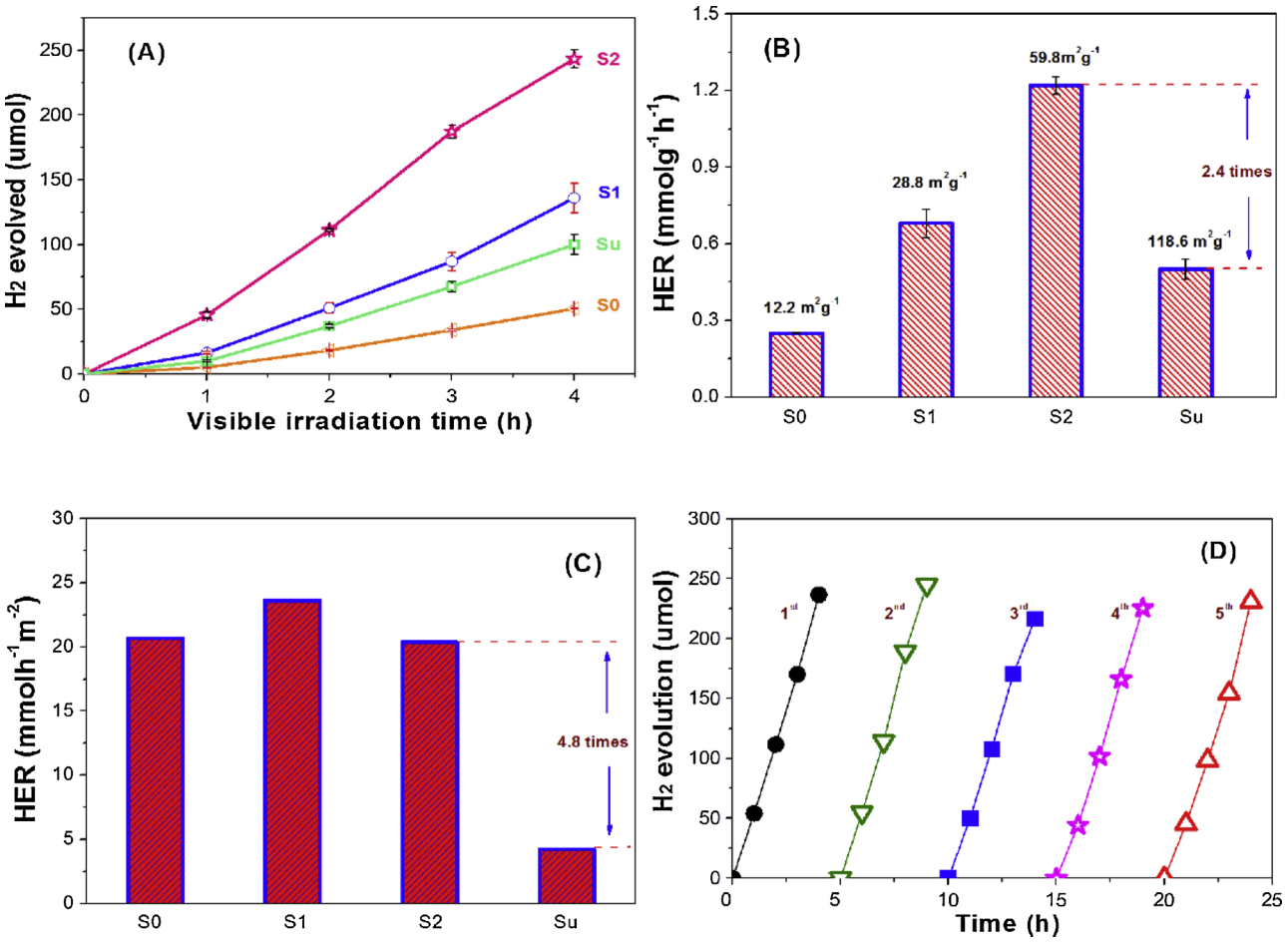

Fig. 9. Dependence of hydrogen production as irradiation time (A), the comparison of the hydrogen evolution rate (HER) of the photocatalyst in unit of weight (B) and surface area (C), and repeating experiments on hydrogen production using S2 as photocatalyst (D).

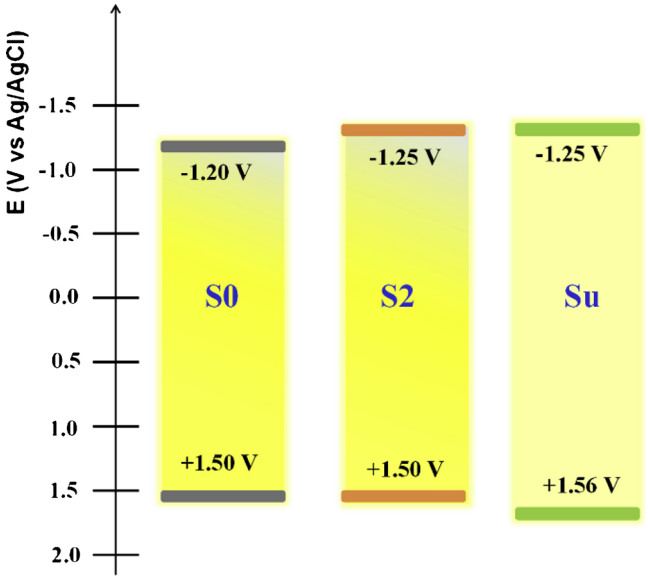

Fig. 10. Comparison of the band structures between S0, S2 and Su samples.

accompanying with small amount of O, with binding energies of 288, 398 and 531 eV, respectively. According to the XPS characterization results, the molar ratio of C/N follows an increase order of S0 (0.639) < S2 (0.646) < Su (0.661), reflecting the improved polymerization of gCN.

High resolution XPS spectrum of C1 s can be deconvoluted into two Gaussian peaks. The larger peak with binding energy of 287.4 eV corresponds to sp^2 C atoms bonded to N inside the aromatic structure of gCN, while the smaller peak with binding energy of 284.6 eV originates from the adventitious hydrocarbon from the XPS instrument itself (Fig. 7B). The high resolution XPS spectra of N 1 s contain peaks at 398.0, 399.6 and 400.5 eV, which are attributed to C═N–C, N-(C_3) and amine groups of gCN photocatalyst, respectively (Fig. 7C). In addition, a small peak with binding energy of 403.4 eV is also observed in high resolution XPS spectrum in N 1 s region, which can be ascribed to highly oxidized chain terminations in the polymeric gCN photocatalyst [50]. The XPS spectra in O 1 s region can be deconvoluted into two peaks with binding energies of 529.1 and 531.8 eV (Fig. 7D). The former originates from oxidized carbon, while the latter comes from the hydroxyl groups of the highly oxidized moieties [45].

3.6. Nitrogen sorption isotherms

Fig. 8 compares the nitrogen adsorption-desorption isotherms of gCN photocatalysts. When compared with that of bulk gCN sample, the adsorption isotherm of gCN-NSs shifts upward, indicating its enlarged BET surface area. The BET surface area of S2 is measured to be 59.8 $m^2 g^{-1}$, 4.9 times higher than that of S0 (12.2 $m^2 g^{-1}$). S2 sample exhibits type H3 hysteresis loop, which is generally associated with plate-like particles, consistent with its sheet-like morphology (Fig. 2) [41]. Due to the exfoliation of gCN, the pore volume of S2 sample (0.282 $cm^3 g^{-1}$) is 5.0 times higher than that of S0 sample (only 0.056 $cm^3 g^{-1}$). The enlarged BET surface area and increased pore

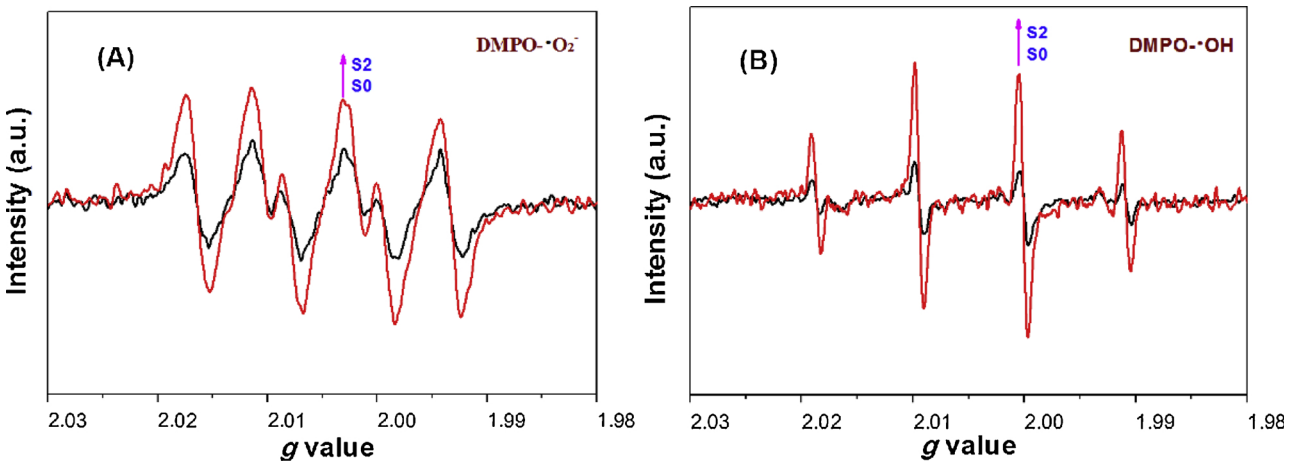

Fig. 11. Comparison of the DMPO spin-trapping ESR spectra between bulk gCN (S0 sample) and gCN-NSs (S2 sample) that was recorded at ambient temperature in methanol solutions for DMPO-·OOH/O_2·$^-$ (A) and in aqueous for DMPO-·OH (B).

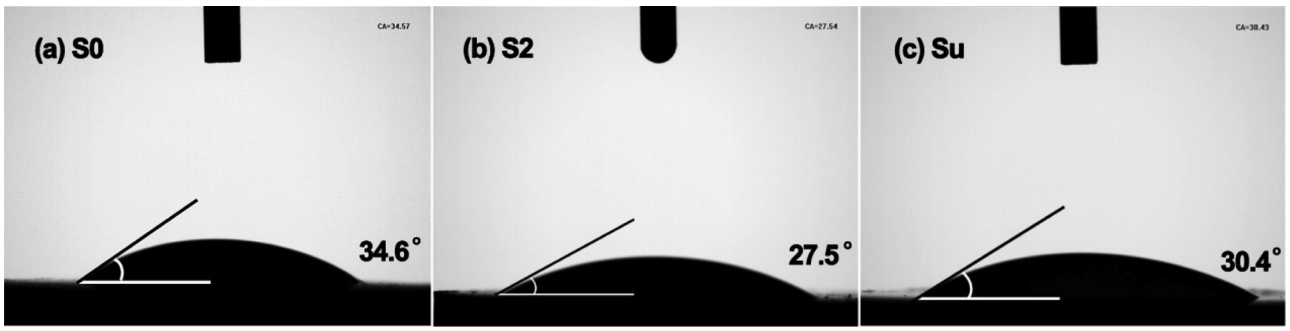

Fig. 12. Water contact angle on the surface of S0 (a), S2 (b) and Su (c) gCN sample.

volume will facilitate the adsorption/diffusion of substrate/photo-generated carriers, enhancing the photocatalytic reaction [51].

3.7. Photocatalytic hydrogen production

Water splitting to produce hydrogen under visible light irradiation was used to evaluate the photocatalytic activity of the prepared gCN photocatalysts. Control experimental result shows that, little H_2 gas can be detected in the absence of any photocatalyst (not shown here). However, the volume of hydrogen gas is found to steady increase with extension the irradiation time in the presence of gCN (Fig. 9A), and S2 gCN-NSs exhibits the highest photoreactivity with an hydrogen production rate of 1.22 mmolg^{-1} h^{-1}, which is 4.9 times higher than that of S0 bulk gCN sample (0.25 mmolg^{-1} h^{-1}). On considering that gCN-NSs (Su sample), that is prepared from polymerization of urea, has similar sheet-like structure, we also measured its water splitting property. It was found that the hydrogen production rate of Su sample is only 0.50 mmolg^{-1} h^{-1}, 41.0% of S2 gCN-NSs (Fig. 9B).

Please note that Su sample exhibits the largest BET surface area (118.6 m^2 g^{-1}) among all the prepared gCN photocatalysts, which is almost 2 times higher than that of S2 gCN-NSs (59.8 m^2 g^{-1}). That was to say, S2 gCN-NSs prepared by polymerization of amidinourea exhibits overwhelming better specific photocatalytic performance than gCN-NSs synthesized by polymerization of urea. The specific photoreactivity of gCN in unit of surface area for S2 is 20.37 umolh^{-1} m^{-2}, which is 4.8 times higher than that of Su gCN-NSs with a specific hydrogen production rate of only 4.22 umolh^{-1} m^{-2} (Fig. 9C). The apparent quantum yield (AQY) for H_2 evolution was measured using monochromatic LED lamps emitted @ 420 nm. It shows that the AQY of S2 gCN-NSs sample @420 nm was 3.11%, which is 1.3 times higher than that of Su gCN-NSs (2.36%), also confirms the higher photoreactivity of gCN-NSs prepared from the polymerization of amidinourea (see supporting information). This may be due to the broader visible-light-responsive range of S2 sample (see Fig. 4).

The stability of the photocatalyst is of great importance from the viewpoint of practical applications. Therefore, repeating experiments were carried out. It shows that the photocatalytic activity of S2 gCN-NSs is very stable. Even after repeated use for 5 times, its photoreactivity almost keeps unchanged (Fig. 9D).

3.8. Reasons for the high photoreactivity

To determine the band structures of the prepared gCN photocatalysts, we measured the Mott-Schottky curves (Fig. S1), and the CB potentials of S0, S2 and Su samples are -1.20, -1.25 and -1.25 eV, respectively. By combination the characterization results of UV–vis diffuse reflectance spectroscopy, the VB potentials of S0, S2 and Su samples were calculated to be +1.50, +1.50 and + 1.56 eV (Fig. 10). When compared with that of bulk gCN (S0) sample, both the CB potentials of S2 and Su are negatively shifted, which thermodynamically enable the rapid proton reduction to production H_2 [12,52].

Since S2 gCN-NSs exhibits a more efficient separation of photogenerated electron-hole pairs than bulk gCN (Fig. 6) and negatively shifted CB potential (Fig. 10), we can predict that the formation of superoxygen radicals (O_2·$^-$) and hydroxyl radicals (·OH) over illuminated gCN-NSs is more preferable. This was confirmed by ESR radical trapping experimental results. From Fig. 11, it can be seen that both the ESR signals of DMPO-·OOH/O_2·$^-$ and DMPO-·OH adducts for S2 gCN-NSs were much stronger than these for S0 bulk gCN, reflecting the high photoreactivity of gCN-NSs [53,54].

Poor dispersion in water is one of the reasons causing the low photoreactivity of bulk gCN [27]. Water contact angle can reflect the

hydrophilic property of the photocatalyst. Therefore, we also measured the water contact angle of the prepared gCN photocatalysts. The contact angles of S0, S2 and Su samples were measured to be 34.6°, 27.5° and 30.4°, respectively (Fig. 12). The smaller contact angle of S2 reflects the strong interface interaction between water and gCN-NSs photocatalyst, which favors for the dissociation and therefore the hydrogen production. Therefore, it is not strange to see the high photocatalytic activity towards water splitting to produce hydrogen gas.

4. Conclusions

In summary, by using the oxygen-containing precursor of amidinourea, sheet-like gCN (gCN-NSs) were successfully fabricated due to the reduced interaction between π–π stacking layers of gCN. The prepared sheet-like gCN exhibits superior photocatalytic hydrogen production performance under visible light irradiation. The high photocatalytic activity of gCN-NSs prepared by polymerization of amidinourea is attributed to the combined effects of excellent visible-light-responsive range, enlarged BET surface area, reduced recombination rate of photo-generated carriers, negatively shifted CB position and improved hydrophilic property.

Acknowledgments

This work was supported by the National Natural Science Foundation of China (51672312, 21373275, 21503281 & 21571192) and the Fundamental Research Funds for the Central Univsrsity, South-Central University for Nationalities (CZT18016).

Appendix A. Supplementary data

Supplementary material related to this article can be found, in the online version, at doi:https://doi.org/10.1016/j.apcatb.2018.12.044.

References

[1] W.J. Ong, L.L. Tan, Y.H. Ng, S.T. Yong, S.P. Chai, Graphitic carbon nitride ($g\text{-}C_3N_4$)-based photocatalysts for artificial photosynthesis and environmental remediation: are We a step closer to achieving sustainability? Chem. Rev. 116 (2016) 7159–7329.

[2] L. Shi, Z. Li, K. Marcus, G.Z. Wang, K. Liang, W.H. Niu, Y. Yang, Integration of Au nanoparticles with a $g\text{-}C_3N_4$ based heterostructure: switching charge transfer from type-II to Z-scheme for enhanced visible light photocatalysis, Chem. Commun. 54 (2018) 3747–3750.

[3] Z.L. Xu, C.S. Zhuang, Z. Zou, J.Y. Wang, X.C. Xu, T.Y. Peng, Enhanced photocatalytic activity by construction of a TiO_2/carbon nitride nanosheets heterostructure with high surface area via direct interfacial assembly, Nano Res. 10 (2017) 2193–2209.

[4] F. Chang, Y.C. Xie, C.L. Li, J. Chen, J.R. Luo, Xu.F. Hu, J.W. Shen, A facile modification of $g\text{-}C_3N_4$ with enhanced photocatalytic activity for degradation of methylene blue, Appl. Surf. Sci. 280 (2013) 967–974.

[5] S.J. He, Q.F. Rong, H.Y. Niu, Y.Q. Cai, Construction of a superior visible-light-driven photocatalyst based on a C_3N_4 active centrephotoelectron shift platform-electron withdrawing unit triadic structure covalent organic framework, Chem. Commun. 53 (2017) 9636–9639.

[6] Z.G. Liu, G. Wang, H.S. Chen, P. Yang, An amorphous/crystalline $g\text{-}C_3N_4$ homojunction for visible light photocatalysis reactions with superior activity, Chem. Commun. 54 (2018) 4720–4723.

[7] Q.Q. Liu, J.Y. Shen, X.F. Yang, T.R. Zhang, H. Tang, 3D reduced graphene oxide aerogel-mediated Z-scheme photocatalytic system for highly efficient solar-driven water oxidation and removal of antibiotics, Appl. Catal. B 232 (2018) 562–573.

[8] W. Cui, J.Y. Li, W.L. Cen, Y.J. Sun, S.C. Lee, F. Dong, Steering the interlayer energy barrier and charge flow via bioriented transportation channels in $g\text{-}C_3N_4$: enhanced photocatalysis and reaction mechanism, J. Catal. 352 (2017) 351–360.

[9] Y.H. Li, K.L. Lv, W.K. Ho, Z.W. Zhao, H. Yu, Enhanced visible-light photo-oxidation of nitric oxide using bismuth-coupled graphitic carbon nitride composite heterostructures, Chin. J. Catal. 38 (2017) 321–329.

[10] G.H. Dong, D.L. Jacobs, L. Zang, C.Y. Wang, Carbon vacancy regulated photoreduction of NO to N_2 over ultrathin $g\text{-}C_3N_4$ nanosheets, Appl. Catal. B 218 (2017) 515–524.

[11] Y.M. He, L.H. Zhang, B.T. Teng, M.H. Fan, A new application of Z-scheme Ag_3PO_4/$g\text{-}C_3N_4$ composite in converting CO_2 to fuel, Environ. Sci. Technol. 49 (2015) 649–656.

[12] Y.F. Li, M. Yang, Y. Xing, X.C. Liu, Y. Yang, X. Wang, S.Y. Song, Preparation of carbon-rich $g\text{-}C_3N_4$ nanosheets with enhanced visible light utilization for efficient photocatalytic hydrogen production, Small 13 (2017) 1701552.

[13] Y.J. Ma, Z.M. Wang, X.F. Xu, J.Y. Wang, Review on porous nanomaterials for adsorption and photocatalytic conversion of CO_2, Chin. J. Catal. 38 (2017) 1956–1969.

[14] D.F. Xu, B. Cheng, W.K. Wang, C.J. Jiang, J.G. Yu, Ag_2CrO_4/$g\text{-}C_3N_4$/graphene oxide ternary nanocomposite Z-scheme photocatalyst with enhanced CO_2 reduction activity, Appl. Catal. B 231 (2018) 368–380.

[15] F. Chen, H. Yang, W. Luo, P. Wang, H.G. Yu, Selective adsorption of thiocyanate anions on Ag-modified $g\text{-}C_3N_4$ for enhanced photocatalytic hydrogen evolution, Chin. J. Catal. 38 (2017) 1990–1998.

[16] J. Jiang, S.W. Cao, C.L. Hu, C.H. Chen, A comparison study of alkali metal-doped $g\text{-}C_3N_4$ for visible-light photocatalytic hydrogen evolution, Chin. J. Catal. 38 (2017) 1981–1989.

[17] X.B. Li, A.F. Masters, T. Maschmeyer, Polymeric carbon nitride for solar hydrogen production, Chem. Commun. 53 (2017) 7438–7446.

[18] P.F. Xia, M.J. Liu, B. Cheng, J.G. Yu, L.Y. Zhang, Dopamine modified $g\text{-}C_3N_4$ and its enhanced visible-light photocatalytic H_2-production activity, ACS Sust. Chem. Eng. 6 (2018) 8945–8953.

[19] S. Fang, Y. Xia, K.L. Lv, Q. Li, J. Sun, M. Li, Effect of carbon-dots modification on the structure and photocatalyticactivity of $g\text{-}C_3N_4$, Appl. Catal. B 185 (2016) 225–232.

[20] S. Fang, K.L. Lv, Q. Li, H.P. Ye, D.Y. Du, M. Li, Effect of acid on the photocatalytic degradation of rhodamine B over $g\text{-}C_3N_4$, Appl. Surf. Sci. 358 (2015) 336–342.

[21] J.S. Cheng, Z. Hu, K.L. Lv, X.F. Wu, Q. Li, Y.H. Li, X.F. Li, J. Sun, Drastic promoting the visible photoreactivity of layered carbon nitride by polymerization of dicyandiamide at high pressure, Appl. Catal. B 232 (2018) 330–339.

[22] Z.X. Zeng, K.X. Li, K. Wei, Y.H. Dai, L.S. Yan, H.Q. Guo, X.B. Luo, Fabrication of porous $g\text{-}C_3N_4$ and supported porous $g\text{-}C_3N_4$ by a simple precursor pretreatment strategy and their efficient visible-light photocatalytic activity, Chin. J. Catal. 30 (2017) 498–508.

[23] W.D. Zhang, Z.W. Zhao, F. Dong, Y.X. Zhang, Solvent-assisted synthesis of porous $g\text{-}C_3N_4$ with efficient visible-light photocatalytic performance for NO removal, Chin. J. Catal. 38 (2017) 372–383.

[24] Y.H. Li, W.K. Ho, K.L. Lv, B.C. Zhu, S.C. Lee, Carbon vacancy-induced enhancement of the visible light-driven photocatalytic oxidation of NO over $g\text{-}C_3N_4$ nanosheets, Appl. Surf. Sci. 430 (2018) 380–389.

[25] K. Pandiselvi, H.F. Fang, X.B. Huang, J.Y. Wang, X.C. Xu, T. Li, Constructing a novel carbon nitride/polyaniline/ZnO ternary heterostructure with enhanced photocatalytic performance using exfoliated carbon nitride nanosheets as supports, J. Hazard. Mater. 314 (2016) 67–77.

[26] P. Niu, L.L. Zhang, G. Liu, H.M. Cheng, Graphene-like carbon nitride nanosheets for improved photocatalytic activities, Adv. Funct. Mater. 22 (2012) 4763–4770.

[27] N.N. Meng, J. Ren, Y. Liu, Y. Huang, T. Petit, B. Zhang, Engineering oxygen-containing and amino groups into twodimensional atomically-thin porous polymeric carbon nitrogen for enhanced photocatalytic hydrogen production, Energy Environ. Sci. 11 (2018) 566–571.

[28] H.H. Ou, L.H. Lin, Y. Zheng, P.J. Yang, Y.X. Fang, X.C. Wang, Tri-s-triazine-based crystalline carbon nitride nanosheets for an improved hydrogen evolution, Adv. Mater. 29 (2017) 1700008.

[29] X.D. Zhang, X. Xie, H. Wang, J.J. Zhang, B.C. Pan, Y. Xie, Enhanced photoresponsive ultrathin graphitic-phase C_3N_4 nanosheets for bioimaging, J. Am. Chem. Soc. 135 (2013) 18–21.

[30] S.B. Yang, Y.J. Gong, J.S. Zhang, L. Zhan, L.L. Ma, Z.Y. Fang, R. Vajtai, X.C. Wang, P.M. Ajayan, Exfoliated graphitic carbon nitride nanosheets as efficient catalysts for hydrogen evolution under visible light, Adv. Mater. 25 (2013) 2452–2456.

[31] Z.M. Xue, F.J. Liu, J.Y. Jiang, J.F. Wang, T.C. Mu, Scalable and super-stable exfoliation of graphitic carbon nitride in biomass-derived γ-valerolactone: enhanced catalytic activity for the alcoholysis and cycloaddition of epoxides with CO_2, Green. Chem. 19 (2017) 5041–5045.

[32] Q. Han, F. Zhao, C.G. Hu, L.X. Lv, Z.P. Zhang, N. Chen, L.T. Qu, Facile production of ultrathin graphitic carbon nitride nanoplatelets for efficient visible-light water splitting, Nano Res. 8 (2015) 1718–1728.

[33] J.J. Ji, J. Wen, Y.F. Shen, Y.Q. Lv, Y.L. Chen, S.Q. Liu, H.B. Ma, Y.J. Zhang, Simultaneous noncovalent modification and exfoliation of 2D carbon nitride for enhanced electrochemiluminescent biosensing, J. Am. Chem. Soc. 139 (2017) 11698–11706.

[34] D.J. Martin, K.P. Qiu, S.A. Shevlin, A.D. Handoko, X.W. Chen, Z.X. Guo, J.W. Tang, Highly efficient photocatalytic H_2 evolution from Water using visible light and structure-controlled graphitic carbon nitride, Angew. Chem. Int. Ed. 53 (2014) 9240–9245.

[35] Y.W. Zhang, J.H. Liu, G. Wu, W. Chen, Porous graphitic carbon nitride synthesized via direct polymerization of urea for efficient sunlight-driven photocatalytic hydrogen production, Nanoscale 4 (2012) 5300–5303.

[36] J.H. Oh, J.M. Lee, Y.J. Yoo, J.H. Kim, S.J. Hwang, S.J. Park, New insight of the photocatalytic behaviors of graphitic carbonnitrides for hydrogen evolution and their associations with grain size,porosity, and photophysical properties, Appl. Catal. B 218 (2017) 349–358.

[37] H.C. Lan, L.L. Li, X.Q. An, F. Liu, C.B. Chen, H.J. Liu, J.H. Qu, Microstructure of carbon nitride affecting synergetic photocatalytic activity: hydrogen bonds vs. structural defects, Appl. Catal. B 204 (2017) 49–57.

[38] M.A. Niaz, A.A. Khan, Kinetics and mechanism of alkaline hydrolysis of malonamide and dicyandiamide, Ind. J. Chem. 30 (1991) 144–147.

[39] A.J. Belsky, T.B. Brill, spectroscopy of hydrothermal reactions. 9. IR and raman spectroscopy of hydrolysis and self-reaction of cyanamide and dicyandiamide at 130-270 °C and 275 bar, J. Phys. Chem. A 102 (1998) 4509–4516.

[40] W. Ding, S.Q. Liu, Z. He, One-step synthesis of graphitic carbon nitride nanosheets for efficient catalysis of phenol removal under visible light, Chin. J. Catal. 38 (2017)

1711–1718.
[41] Z.A. Huang, Q. Sun, K.L. Lv, Z.H. Zhang, M. Li, B. Li, Effect of contact interface between TiO_2 and g-C_3N_4 on the photoreactivity of g-C_3N_4/TiO_2 photocatalyst: (001) vs (101) facets of TiO2, Appl. Catal. B 164 (2015) 420–427.
[42] L.J. Fang, X. Lu Wang, J.J. Zhao, Y.H. Li, Y.L. Wang, X.L. Du, Z.F. He, H.D. Zeng, H.G. Yang, One-step fabrication of porous oxygen-doped g-C_3N_4 with feeble nitrogen vacancies for enhanced photocatalytic performance, Chem. Commun. 52 (2016) 14408–14411.
[43] Y.H. Li, K.L. Lv, W.K. Ho, F. Dong, X.F. Wu, Y. Xia, Hybridization of rutile TiO_2 ($rTiO_2$) with g-C_3N_4 quantum dots (CN QDs): an efficient visible-light-driven Z-scheme hybridized photocatalyst, Appl. Catal. B 202 (2017) 611–619.
[44] M.J. Liu, P.F. Xia, L.Y. Zhang, B. Cheng, J.G. Yu, Enhanced photocatalytic H_2-production activity of g-C_3N_4 nanosheets via optimal photodeposition of Pt as co-catalyst, ACS Sust. Chem. Eng. 6 (2018) 10472–10480.
[45] P.F. Xia, B.C. Zhu, B. Cheng, J.G. Yu, J.S. Xu, 2D/2D g-C_3N_4/MnO_2 nanocomposite as a direct Z-scheme photocatalyst for enhanced photocatalytic activity, ACS Sust. Chem. Eng. 6 (2018) 965–973.
[46] Y.H. Li, X.F. Wu, W.K. Ho, K.L. Lv, Q. Li, M. Li, S.C. Lee, Graphene-induced formation of visible-light-responsive SnO_2-Zn_2SnO_4 Z-scheme photocatalyst with surface vacancy for the enhanced photoreactivity towards NO and acetone oxidation, Chem. Eng. J. 336 (2018) 200–210.
[47] G.S. Li, Z.C. Lian, W.C. Wang, D.Q. Zhang, H.X. Li, Nanotube-confinement induced size-controllable g-C_3N_4 quantum dots modified single-crystalline TiO_2 nanotube arrays for stable synergetic photoelectrocatalysis, Nano Energy 19 (2016) 446–454.
[48] C.Y. Feng, Y.C. Deng, L. Tang, G.M. Zeng, J.J. Wang, J.F. Yu, Y.N. Liu, B. Peng, H.P. Feng, J.J. Wang, Core-shell Ag_2CrO_4/N-GQDs@g-C_3N_4 composites with anti-photocorrosion performance for enhanced full-spectrum-light photocatalytic activities, Appl. Catal. B 239 (2018) 525–536.
[49] L. Tang, C.Y. Feng, Y.C. Deng, G.M. Zeng, J.J. Wang, Y.N. Liu, H.P. Feng, J.J. Wang, Enhanced photocatalytic activity of ternary Ag/g-C_3N_4/$NaTaO_3$ photocatalysts under wide spectrum light radiation: The high potential band protection mechanism, Appl. Catal. B 230 (2018) 102–114.
[50] K.L. Corp, C.W. Schlenker, Ultrafast spectroscopy reveals electron-transfer cascade that improves hydrogen evolution with carbon nitride photocatalysts, J. Am. Chem. Soc. 139 (2017) 7904–7912.
[51] R.W. Yang, J.H. Cai, K.L. Lv, X.F. Wu, W.G. Wang, Z.H. Xu, M. Li, Q. Li, W.Q. Xu, Fabrication of TiO_2 hollow microspheres assembly from nanosheets (TiO_2-HMSs-NSs) with enhanced photoelectric conversion efficiency in DSSCs and photocatalytic activity, Appl. Catal. B 210 (2017) 184–193.
[52] G.G. Zhang, G.S. Li, Z.A. Lan, L.H. Lin, A. Savateev, T. Heil, S. Zafeiratos, X.C. Wang, M. Antonietti, Optimizing optical absorption, exciton dissociation, and charge transfer of a polymeric carbon nitride with ultrahigh solar hydrogen production activity, Angew. Chem. Int. Ed. 56 (2017) 13445–13449.
[53] L. Tian, X.F. Yang, Q.Q. Liu, F.Q. Qu, H. Tang, Anchoring metal-organic framework nanoparticles on graphitic carbon nitrides for solar-driven photocatalytic hydrogen evolution, Appl. Surf. Sci. 455 (2018) 403–409.
[54] W. Liu, J. Shen, Q.Q. Liu, X.F. Yang, H. Tang, Porous MoP network structure as co-catalyst for H_2 evolution over g-C_3N_4 nanosheets, Appl. Surf. Sci. 462 (2018) 822–830.